Heterometallic [Cu-O-M]$^{2+}$ Active Sites for Methane C-H Activation in Zeolites: Stability, Reactivity, Formation Mechanism and Relationship to Other Active Sites

Olajumoke Adeyiga[#], Dipak Panthi[#] and Samuel O. Odoh*

Department of Chemistry, University of Nevada Reno, 1664 N. Virginia Street, Reno, NV 89557-0216

Email Addresses:

sodoh@unr.edu

ABSTRACT: The formation and reactivities of [Cu-O-M]$^{2+}$ species (M = Ti-Cu, Zr-Mo and Ru-Ag) in metal-exchanged zeolites, as well as stabilities of these species towards autoreduction by O_2 elimination are investigated with density functional theory. These species were investigated in zeolite mordenite in search of insights into active site formation mechanisms, relationship between stability and reactivity as well as discovery of heterometallic species useful for isothermal methane-to-methanol conversion (MMC). Several [Cu-O-M]$^{2+}$ species (M = Ti-Cr and Zr-Mo) are substantially more stable than [Cu$_2$O]$^{2+}$. Other [Cu-O-M]$^{2+}$ species, (M = Mn-Ni and Ru-Ag) have similar formation energies as [Cu$_2$O]$^{2+}$, to within ±10 kcal/mol. Interestingly, only [Cu-O-Ag]$^{2+}$ is more active for methane activation than [Cu$_2$O]$^{2+}$. [Cu-O-Ag]$^{2+}$ is however more susceptible to O_2 elimination. By considering the formation energies, autoreduction, cost and activity towards the methane C-H bond, we can only conclude that [Cu$_2$O]$^{2+}$ is best suited for MMC. Formation of [Cu$_2$O]$^{2+}$ is initiated by proton transfer from aquo ligands to the framework and proceeds mostly via dehydration steps. Its μ-oxo bridge is formed via water-assisted condensation of two hydroxo groups. To evaluate the relationship between [Cu$_2$O]$^{2+}$ and other active sites, we also examined the formation energies of other species. The formation energies follow the trend: isolated [Cu-OH]$^{+}$ < paired [Cu-OH]$^{+}$ < [Cu$_2$O]$^{2+}$ < [Cu$_3$O$_3$]$^{2+}$. Inclusion of Gibbs free-energy corrections indicate activation temperatures of 257, 307 and 327 and 331 °C for isolated [Cu-OH]$^{+}$, paired [Cu-OH]$^{+}$, [Cu$_2$O]$^{2+}$ and [Cu$_3$O$_3$]$^{2+}$, respectively. The provocative nature of the lower-than-expected activation temperature for isolated [Cu-OH]$^{+}$ species is discussed.

1. INTRODUCTION

Methane is the major component of natural gas and activation of methane to produce commodity chemicals has generated significant interest. This is due to the desire to exploit natural gas reserves and address environmental concerns from widespread flaring of natural gas.[1-3] Currently, methane utilization involves energy-intensive pathways via generation of syngas.[4-6] These routes are used on a large scale but are not economically feasible for small-scale facilities, such as at remote gas fields. Hence, new approaches for methane conversion are of interest. Foremost amongst these is the direct selective oxidation of methane to methanol.[7-11]

Direct oxidation of methane to methanol occurs naturally in microorganisms, catalyzed by methane monooxygenase (MMO) enzymes. These contain di-iron and di-copper active centers.[12-14] As such, development of artificial catalysts for methane activation has focused on mimicking the structures of these active sites.[15] Zeolites have been considered as good candidates for hosting metallic centers that are reminiscent of those in MMO enzymes.[16-18] Many zeolites have been studied for this purpose. However, copper-exchanged mordenite (Cu-MOR) zeolites are some of the most interesting ones. Their large pores facilitate desorption of reaction products from copper active sites.[7, 19-21] Methane to methanol conversion, MMC, in zeolites like Cu-MOR is often carried out in a stepwise fashion. The process begins with generation of copper active sites under oxidizing conditions. This is followed by contact with methane, leading to formation of intra-zeolite methoxy intermediates. Recent work has revealed that the methoxy intermediates are stabilized at Brønsted acid sites.[22-25] These methoxy groups are extracted as methanol in a third step, with water. At the end of each loop, the active sites are regenerated via thermal treatment with oxidants like O_2, H_2O and H_2O_2.[26-28] The activation and regeneration steps occur at 350-550 °C, while methane activation is carried out near 200 °C.

Active site species responsible for MMC in copper-exchanged zeolites have been extensively studied. Some of the proposed active sites are $[Cu\text{-}OH]^+$, $[Cu_2O]^+$ and $[Cu_3O_3]^{2+}$. Many studies have focused on the relationships between these active sites, their speciation in various zeolites and under various synthesis conditions, their spectroscopic properties and their reactivities with methane.[29-33] Crucially, there is renewed interest in the capabilities of spectroscopic techniques for investigating the nuclearity of copper-oxo active sites.[26, 29-32, 34, 35] Additionally, there is an ongoing debate regarding preparation of zeolites with unique $[Cu_3O_3]^{2+}$ sites.[13, 26, 33, 36] In many cases, experimental investigations of copper-exchanged zeolites have been complemented with quantum-

mechanical computations. However, the literature contains very little theoretical investigations of the pathway for forming the copper active sites during the activation step.[19, 37] In this work, we investigate the formation pathway for mono-(μ-oxo) dicopper $[Cu_2O]^{2+}$ active sites. We also investigate the extent to which the thermodynamics for forming $[Cu_2O]^{2+}$ species provide insights into activation temperatures. We focus on $[Cu_2O]^{2+}$ as it is the only spectroscopically verified and the most ubiquitous active site motif under typical activation conditions.[38]

Several workers have used density functional theory (DFT)[39, 40] calculations to examine the stabilities and reactivities of heterobimetallic $[Cu-O-M]^{2+}$ active sites in various zeolites. These sites are analogous to $[Cu_2O]^{2+}$ but with one copper center replaced with another metal. Zheng et al. examined how methane C-H activation barriers of $[Cu-O-M]^{2+}$ species are affected by the electronic structure properties of the μ-oxo site as well as the Cu-O-M bond angle in ZSM-5. They considered cases where M is Ag, Au, Cu or Zn.[41] Wang et al. performed a similar analysis for the MAZ zeolite using $[Cu-O-M]^{2+}$ species where M = Pd, Pt, Fe, Co, Ni, Au and Ag.[42] Kulkarni et al. also examined methane C-H reactivities of $[Cu-O-Co]^{2+}$, $[Cu_2O]^{2+}$, $[Cu-O-Fe]^{2+}$ and $[Cu-O-Ni]^{2+}$.[43] The stabilities of these $[Cu-O-M]^{2+}$ active sites are generally referenced against an oxidant (for example O_2 or N_2O) and mono-cations bound to the zeolite, Cu^+ and M^+. Thus, the formation energies of $[Cu-O-M]^{2+}$ sites were nearly always negative, exothermic. However, typical experimental setups involve calcining at high temperatures, sometimes initially in helium gas followed by exposure to oxidants. As such, modeling the relative stabilities of $[Cu_2O]^{2+}$ and $[Cu-O-M]^{2+}$ species must capture the endothermicity of the combined dehydration and oxidation steps. It is for this reason that we previously referenced the formation of various active sites against $[Cu(H_2O)_6]^{2+}$.[24] This approach ensures that formation of the metal-oxo active sites is an endothermic process, thus allowing estimations of activation temperatures. It also aids quantitative descriptions of contributions from the dehydration and oxidation steps.

Lastly, van Bokhoven et al. have reported successful MMC under isothermal conditions near 200 °C.[44] In these experiments, the copper-exchanged zeolite is activated at the same temperature for reaction with methane. This is a path for removing thermal and temporal gradients between the activation and methane loading steps. However at 200 °C, it is generally thought that dehydrated $[Cu-OH]^+$, $[Cu_2O]^+$ and $[Cu_3O_3]^{2+}$ active sites cannot exist. For this reason, there is significant interest in determining the natures of the copper species that engender MMC under isothermal conditions. In this work, we take a somewhat different approach. We consider whether tuning the

heterometallic nature of the $[Cu-O-M]^{2+}$ sites could lead to species that are sufficiently stable as to be activated near 200 °C. We do this by considering M as $3d$ (Ti-Ni) or $4d$ (Zr-Mo and Ru-Ag) transition metals. Additionally, heterometallic active sites like the $[Cu-O-M]^{2+}$ species are considered interesting for chemical catalysis, especially in the spirit of mimicking heterobimetallic cores found in some metalloenzymes.[45-50] Here, we access the usefulness of the $[Cu-O-M]^{2+}$ species with DFT calculations of their formation, auto-reduction as well as their reactivities with methane. These computations will save great time in experimental investigations.

2. COMPUTATIONAL DETAILS

Periodic DFT Calculations: Periodic calculations were carried out with the Quantum Espresso software suite, version 6.4.1.[51, 52] We used periodic cells of the proton-form of zeolite mordenite, H_4MOR. In this system, there are four aluminate tetrahedra, with their charges balanced by four protons, Figure 1. The Si/Al ratio in H_4MOR is 11/1, matching well with previously studied experimental systems.[36] There are two aluminate tetrahedra at the mouth of the eight-membered
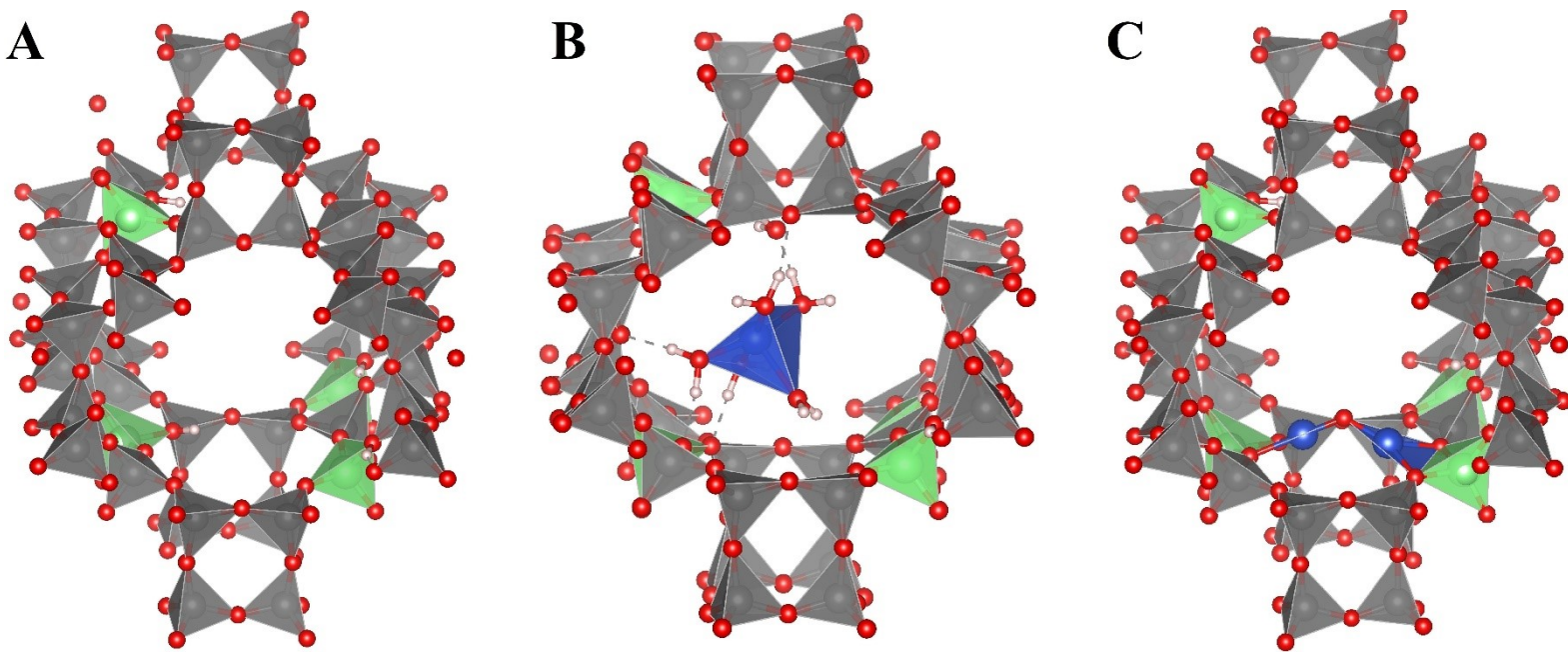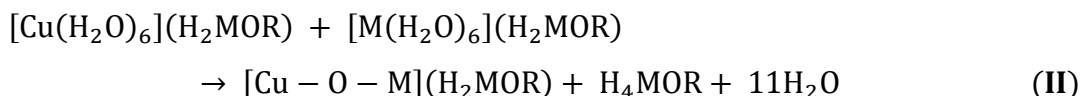

Figure 1: Structures of **(A)** H_4MOR, **(B)** $[Cu(H_2O)_6](H_2MOR)$ and **(C)** $[Cu_2O](H_2MOR)$. O, Si, Al and Cu atoms are represented with red, grey, green and blue polyhedra, respectively. Locations of the charge-balancing protons are visible and the aluminates conform to Lowenstein's rule.

ring, 8MR. These are used as the sites for the copper-oxo active sites, in agreement with previous reports.[24, 25, 34, 36, 53] The optimized structure of H_4MOR was used to construct $[Cu(H_2O)_6](H_2MOR)$ and $[Cu_2O](H_2MOR)$ species, Figure 1. In these, 2 protons are replaced by

$[Cu(H_2O)_6]^{2+}$ and $[Cu_2O]^{2+}$, respectively. All other intermediate structures were also created from H$_4$MOR. Additionally, for the species shown in Figure 1, the two aluminates in the bottom 8MR are separated by 3 silicates. Projected augmented wave pseudopotentials were used with charge density and wavefunction cut-offs set to 350.0 Ry and 50.0 Ry respectively.[54, 55] The PBE density functional[56] was employed with dispersion corrections included using the D3 scheme[57, 58] (PBE-D3). Sampling of the Brillouin zone was set to the Γ point. For transition state searches, the nudge elastic band (NEB) approach was used.[59] There are 6-8 images between each set of reactant and intermediate/product endpoints.

Formation Reaction: Formation energy of $[Cu_2O]^{2+}$ sites can be obtained by considering **I**. In this reaction, the copper-oxo site is formed via dehydration and oxidation of $[Cu(H_2O)_6](H_2MOR)$. $[Cu(H_2O)_6](H_2MOR)$ is a good the starting point for activation of copper-zeolites under near-neutral pH conditions.[24] With **I** we are referencing the stability of $[Cu_2O]^{2+}$ active sites against $[Cu(H_2O)_6]^{2+}$. There is a universal consensus that Cu assumes a hexaaquo octahedral coordination after ion-exchange with zeolites in acidic pH conditions.[36, 60-62] Thus, it is eminently reasonable to reference the stabilities of the copper active sites against the hexaaquo complex. Previous workers have considered the stabilities of copper-oxo species relative to bulk copper oxides, Cu$^+$ or [Cu-OH]$^+$. For the heterometallic analogues of the $[Cu_2O]^{2+}$ site, we use reaction **II**. As stated earlier, M includes all 3d transition metals (Ti-Ni) as well as all 4d transition metals (Zr-Ag), except for Tc. We note that Lamberti et al. have previously reported that thermal activation of copper species in MOR causes desorption of water molecules.[63] Dehydration is accompanied by aggregation into $[Cu_2O]^{2+}$ moieties. **I** and **II** conform to these experimental observations.

$$2[Cu(H_2O)_6](H_2MOR) \rightarrow [Cu_2O](H_2MOR) + H_4MOR + 11H_2O \qquad \textbf{(I)}$$

$$[Cu(H_2O)_6](H_2MOR) + [M(H_2O)_6](H_2MOR)$$
$$\rightarrow [Cu-O-M](H_2MOR) + H_4MOR + 11H_2O \qquad \textbf{(II)}$$

Interestingly, the aquo ligands in $[Cu(H_2O)_6](H_2MOR)$ and $[M(H_2O)_6](H_2MOR)$ can be arranged in various ways. Indeed, an octahedral structure as shown in Figure 1 is not necessarily the lowest energy geometry. As such, we initially performed an initial ab initio molecular dynamics, AIMD, simulation on these structures. Details of the AIMD protocol have been previously provided.[34] After a 20 ps equilibration step, we randomly extracted 20 structures over 40 ps simulation time. These were re-optimized Quantum Espresso. The most stable structures for $[Cu(H_2O)_6](H_2MOR)$ and $[M(H_2O)_6](H_2MOR)$ were used to compute reaction energies of **I** and **II**. The considered spin
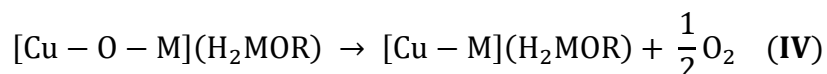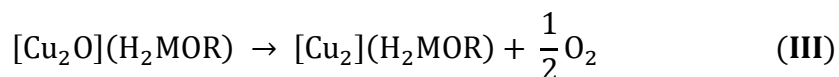
states as well as relative spin state energies of all species involved in **I** and **II** are provided in the supporting information. The ground spin multiplicities of the [Cu-O-M](H$_2$MOR) species are also provided in Table 1.

Table 1: Ground state multiplicities (2S+1) of the [Cu-O-M]$^{2+}$ active sites in the MOR zeolite.

3d	Ti	V	Cr	Mn	Fe	Co	Ni	Cu
	2	3	4	5	4	5	4	0
4d	Zr	Nb	Mo		Ru	Rh	Pd	Ag
	2	3	4		2	1	2	3

To determine the impact of the exchange-correlation functional on the calculated reaction energies, we used the formation of [Cu$_2$O](H$_2$MOR) as a testbed. Single-point calculations on the PBE-D3-optimized structures were performed with rVV10[64, 65] and rev-vdW-DF2.[66] We also re-optimized the geometries with rVV10 for detailed comparison.

Decomposition with Oxygen Elimination: It has been reported that thermal treatment of zeolites containing [Cu$_2$O]$^{2+}$ sites leads to elimination of molecular oxygen, O$_2$.[61, 63] Indeed, autoreduction of Cu^{2+} to Cu$^+$ has been hypothesized to be due to emission of O$_2$ from μ-oxo bridges of [Cu$_2$O]$^{2+}$ active sites.[63] This process is described in reaction **III**. The thermodynamics of **III** has been used to previously gauge the stability of [Cu$_2$O]$^{2+}$ active sites. Here, we extend this to heterometallic species containing all 3d and 4d transition metals, except Tc. Decomposition of the heterometallic species under anaerobic conditions is described by **IV**.

$$[Cu_2O](H_2MOR) \rightarrow [Cu_2](H_2MOR) + \frac{1}{2}O_2 \qquad \textbf{(III)}$$

$$[Cu - O - M](H_2MOR) \rightarrow [Cu - M](H_2MOR) + \frac{1}{2}O_2 \quad \textbf{(IV)}$$

To summarize, these active sites are formed by dehydration and oxidation of aquo Cu^{2+} species, via thermal treatment. These steps are contained in reactions **I-II,** and thus formation energies are appropriately referenced against aquo complexes. However, further thermal treatment of the active sites leads to autoreduction, as seen in **III-IV**. As such, we do not use **III** or **IV** to describe the formation of the active sites, but rather to describe their stability towards O$_2$ elimination. The spin states and relative spin state energies of species involved in **III** and **IV** are also provided in the supporting information.

Cluster-model Calculations: Periodic DFT calculations provide accurate reaction energies for **I-IV**. However, obtaining Gibbs free-energy corrections with periodic DFT is very expensive. As

such, we turn to representative cluster models for obtaining these corrections. Geometry optimizations and vibrational frequency analyses were carried out with cluster models for the isolated [Cu-OH]$^+$, paired [Cu-OH]$^+$, [Cu$_2$O]$^{2+}$ and [Cu$_3$O$_3$]$^{2+}$ active sites in the 8MR of MOR, Figure 2. The terminating oxo sites of the cluster models were capped with protons. The positions of these protons were first optimized and then fixed in all other calculations. These cluster-model calculations were performed at the scalar relativistic level with the Priroda code[67, 68] while using the PBE functional and double-ζ-polarized quality basis sets for the large component and appropriate kinetically balanced basis sets for the small components.[69, 70] Vibrational frequency analyses were carried out with the harmonic approximation. This allows us to obtain Gibbs free-energy corrections at various temperatures (25 - 750 °C).
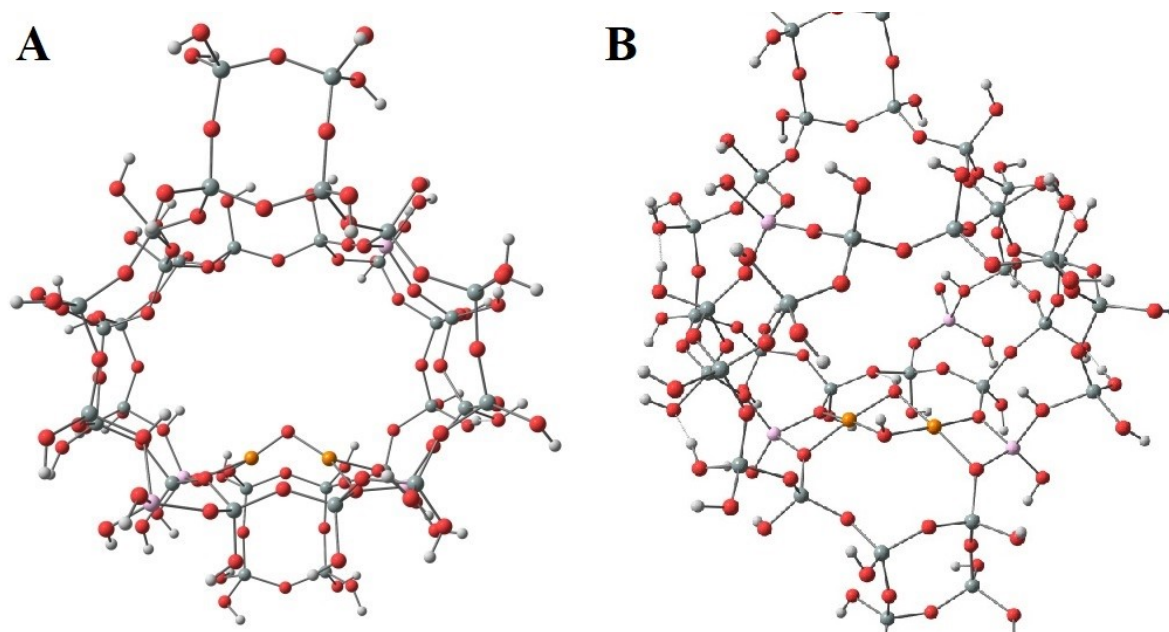

Figure 2: Cluster-model structures of **(A)** [Cu$_2$O]$^{2+}$ and **(B)** paired [Cu-OH]$^+$ in MOR. The latter is slightly rotated to allow easy visualization of the copper site. H, O, Si, Al and Cu atoms are represented with white, red, grey, pink and orange spheres, respectively.

3. RESULTS AND DISCUSSION

We first present the lowest energy structures of the species involved in **I-II**. We then discuss formation energies for [Cu$_2$O]$^{2+}$ and [Cu-O-M]$^{2+}$ active sites. The density functional dependence of the calculated formation energies are also discussed. The stabilities of the [Cu$_2$O]$^{2+}$ and [Cu-O-M]$^{2+}$ sites towards O$_2$ elimination during thermal treatment are then described. This leads us to a description of the detailed mechanism for forming [Cu$_2$O]$^{2+}$ sites. Lastly, the Gibbs free-energy corrections to the formation energy of [Cu$_2$O]$^{2+}$ allows us to compare it to other copper active sites.

3.1. Optimized Structures: For [Cu(H$_2$O)$_6$](H$_2$MOR) and [Cu$_2$O](H$_2$MOR), we considered how the total energy is influenced by the sitings of the aluminate tetrahedra. In the latter, aluminates in the bottom 8MR bind directly to [Cu$_2$O]$^{2+}$. The aluminates can be separated by 2 or 3 silicates, leading to Al-Si-Si-Si-Al, Figure 1, or Al-Si-Si-Al arrangements, Figure 3. In [Cu$_2$O](H$_2$MOR), the total energies are largely indifferent to Al-Si-Si-Al or Al-Si-Si-Si-Al arrangements of the aluminates to which [Cu$_2$O]$^{2+}$ is coordinated.[71] Indeed, species with Al-Si-Si-Al or Al-Si-Si-Si-Al differ only by 0.1-0.9 kcal/mol. For [Cu(H$_2$O)$_6$](H$_2$MOR), structures in which the aluminates of the bottom 8MR possess the Al-Si-Si-Si-Al arrangement are more stable than those with Al-Si-Si-Al arrangement by 3.5-9.5 kcal/mol. Thus, we consider only species with the Al-Si-Si-Si-Al arrangement in all our subsequent discussions.
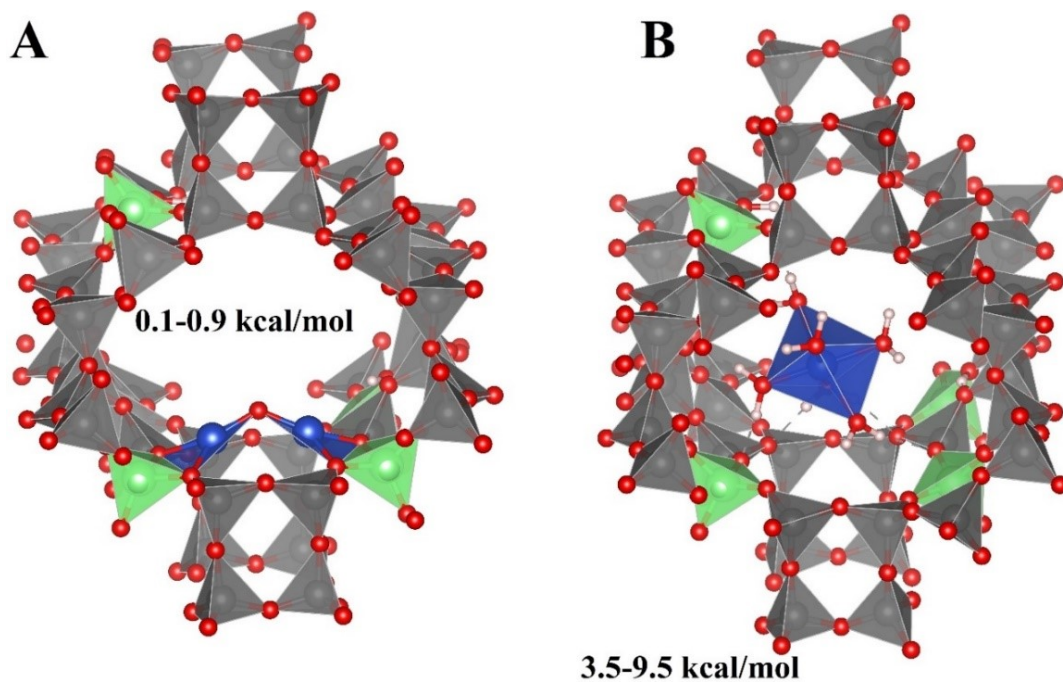
Figure 3: Optimized periodic structures of **(A)** [Cu$_2$O](H$_2$MOR) and **(B)** [Cu(H$_2$O)$_6$](H$_2$MOR) with Al-Si-Si-Al arrangements of the aluminates in the lower 8MR channel.

3.2. Formation Energies: Reaction energies for formation of [Cu$_2$O](H$_2$MOR) via **I** are presented in Table 2. Results for rev-vdW-DF2 and rVV10 were obtained with PBE atomic pseudopotentials. The formation energy for [Cu$_2$O]$^{2+}$ is 222.5 kcal/mol with PBE-D3. With rev-vdW-DF2, the formation energy is 214.8 kcal/mol. This is within 7.7 kcal/mol of PBE-D3. However, with rVV10, we obtain 233.3 kcal/mol, 10.7 kcal/mol higher than for PBE-D3. After re-optimizing the relevant geometries with rVV10, we obtained a reaction energy of 233.2 kcal/mol, Table 2. Overall, deviations due to the choice of exchange-correlation density functional as well as the structural

dynamics of the $[Cu(H_2O)_6](H_2MOR)$ reactants, Figure 3, allow us to estimate that there is likely an error bar of ±15 kcal/mol associated with the calculated formation energies. Importantly, the formation energy for $[Cu_2O]^{2+}$ is always positive, endothermic. Therefore, the temperature must be raised to dehydrate and oxidize $[Cu(H_2O)_6](H_2MOR)$ reactants of reaction **I**. This conforms to experimental protocols. As noted earlier, previous evaluations of the stabilities of copper-oxo active sites have used bulk copper oxides, $[Cu-OH]^{+72}$ or Cu^+ as references. In such cases, the formation reactions were exothermic. These are clearly in disaccordance with experimental practice of activating zeolites by raising the temperature.

Table 2: Calculated formation energies for the $[Cu_2O]^{2+}$ active site.

Structure optimization	Single-point calculation	Reaction energy (kcal/mol)
PBE-D3	PBE-D3	222.5
	rev-vdW-DF2	214.8
	rVV10	233.3
rVV10	rVV10	233.2

The formation energies for heterometallic $[Cu-O-M](H_2MOR)$ species display some trends, Figure 4. $3d$ elements in groups 7-10, Mn-Ni, give formation energies of $[Cu-O-M]^{2+}$ similar to that of $[Cu_2O]^{2+}$. The formation energy of $[Cu-O-Ni]^{2+}$ is 8.1 kcal/mol higher than for $[Cu_2O]^{2+}$. However, the formation energies of $[Cu-O-Mn]^{2+}$, $[Cu-O-Fe]^{2+}$ and $[Cu-O-Co]^{2+}$ are all within 3 kcal/mol of $[Cu_2O]^{2+}$. By contrast, $3d$ elements in groups 4-6, Ti-Cr, yield formation energies below that of $[Cu_2O]^{2+}$. Formation energies of $[Cu-O-Ti]^{2+}$, $[Cu-O-V]^{2+}$ and $[Cu-O-Cr]^{2+}$ are 27.3, 12.5 and 10.0 kcal/mol respectively lower than for $[Cu_2O]^{2+}$.

The formation energies for all $4d$-metal-containing $[Cu-O-M]^{2+}$ species are lower than those of $[Cu_2O]^{2+}$, with Mo, Nb and Zr being the lowest, Figure 4. Indeed, the formation energies of $[Cu-O-Zr]^{2+}$, $[Cu-O-Nb]^{2+}$ and $[Cu-O-Mo]^{2+}$ are 45.2, 39.0 and 31.1 kcal/mol lower than for $[Cu_2O]^{2+}$, respectively. The lower formation energies of these species suggest that they could be candidates for utilization under isothermal conditions. Also, the formation energies of $[Cu-O-Ru]^{2+}$ and $[Cu-O-Rh]^{2+}$ are 6.2 and 10.6 kcal/mol lower than for $[Cu_2O]^{2+}$, respectively. However, heterometallic Ru and Rh sites are not as stable as the Mo, Nb and Zr species. Kulkarni et al. have previously described an inverse correlation between the formation energy of the active site motif and its reactivity towards methane.[19, 43] $[Cu-O-Ru]^{2+}$ and $[Cu-O-Rh]^{2+}$ could thus be the optimal trade-off between stability and reactivity. For this reason, we shall carefully consider $[Cu-O-Cr]^{2+}$, $[Cu-O-$

V]$^{2+}$, [Cu-O-Ti]$^{2+}$, [Cu-O-Mo]$^{2+}$, [Cu-O-Nb]$^{2+}$, [Cu-O-Zr]$^{2+}$, [Cu-O-Ru]$^{2+}$ and [Cu-O-Rh]$^{2+}$ in subsequent discussions.
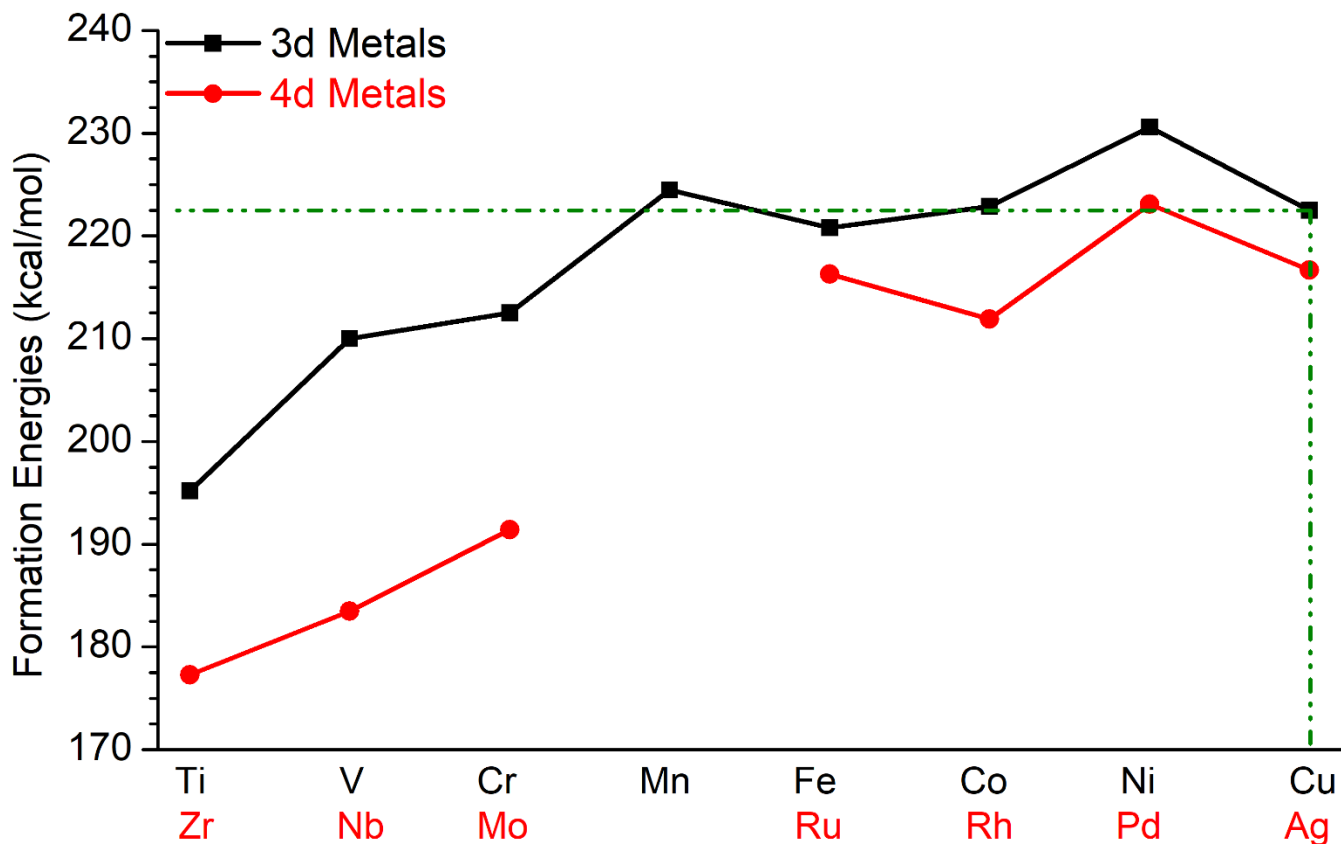
Figure 4: Formation energies of [Cu-O-M](H$_2$MOR) species from [Cu(H$_2$O)$_6$][H$_2$MOR] and [M(H$_2$O)$_6$][H$_2$MOR] species.

3.3. Decomposition via Oxygen Elimination: Reactions **III** and **IV** involve elimination of O$_2$ as well as reduction of Cu^{2+} to Cu$^+$ and M^{2+} to M$^+$. These reduction processes would be favored under anaerobic conditions. In addition to the report of Lamberti et al., this autoreduction process has been widely reported, even in the presence of O$_2$.[61] The reaction energies for **III** and **IV** are presented in Table 3. The calculated O$_2$ elimination energy for [Cu$_2$O]$^{2+}$ is 53.9 kcal/mol. This indicates that [Cu$_2$O]$^{2+}$ is stable against O$_2$ elimination. To achieve autoreduction of the Cu^{2+} sites of [Cu$_2$O]$^{2+}$ to Cu$^+$, the temperature must be raised. This agrees with experimental observations of [Cu$_2$O]$^{2+}$ aggregates prior to signatures for autoreduction, as the temperature is raised.[61, 63, 73] Compared to other 3d [Cu-O-M]$^{2+}$ species, the O$_2$ elimination energy of [Cu$_2$O]$^{2+}$ is the smallest while the one for [Cu-O-Ti]$^{2+}$ is the highest. We therefore see that the active sites are less stable against auto-reduction as one moves down the period. A similar trend occurs for 4d [Cu-O-M]$^{2+}$ species, with [Cu-O-Zr]$^{2+}$ being most stable and [Cu-O-Ag]$^{2+}$ being least stable. Additionally, for

elements in groups 4-8, the $4d$ species are more stable than the $3d$ species towards O_2 elimination by 2.8-12.5 kcal/mol. By contrast, for elements in groups 9-11, the $3d$ species are more resistant

Table 3: Energies, kcal/mol, for O_2 elimination from $[Cu_2O]^{2+}$ and $[Cu-O-M]^{2+}$ active sites.

$3d$	Ti	V	Cr	Mn	Fe	Co	Ni	Cu
	114.9	105.7	88.6	73.1	72.7	71.7	63.7	53.9
$4d$	Zr	Nb	Mo		Ru	Rh	Pd	Ag
	117.7	118.2	101.1		79.5	65.6	45.8	26.1

towards O_2 elimination. In copper-exchanged zeolites, conversion of methane to methanol is achieved with the $Cu^{2+} \rightarrow Cu^+$ redox couple.[74, 75] Thus, active sites that are more resistant against autoreduction would be more useful. Importantly, our 8 species of interest, $[Cu-O-Cr]^{2+}$, $[Cu-O-V]^{2+}$, $[Cu-O-Ti]^{2+}$, $[Cu-O-Mo]^{2+}$, $[Cu-O-Nb]^{2+}$, $[Cu-O-Zr]^{2+}$, $[Cu-O-Ru]^{2+}$ and $[Cu-O-Rh]^{2+}$, provide O_2 elimination energies that are higher than for $[Cu_2O]^{2+}$.

3.4. Reactivity with Methane: The activation barrier fosr the methane C-H bond is often used to evaluate the reactivities of copper-oxo active site. This makes sense in light of our recent report where we found that between methane and formates, the transition state for the first hydrogen atom abstraction step has the highest energy.[25] Thus, the methane C-H activation step is the rate-determining step. We therefore use the barriers associated with this step to evaluate the reactivities of the $[Cu-O-M]^{2+}$ species. We considered two possible routes for methane C-H dissociation. The first involves a radical-like transition state. This has been previously described.[18, 76] The second possibility is a surface-stabilized transition state in which the separated methyl group becomes bound to one of the metal centers.[41, 77, 78] However, prior to discussing the calculated barriers associated with the radical-like and surface-stabilized mechanisms, we first consider the energies of the species formed after methane C-H activation. In Table 4, the energies of the separated- (radical-like pathway) and surface-stabilized- (surface-stabilized pathway) -methyl intermediates are given relative to the adduct complex of methane and the active site.

The separated-methyl intermediate is always less stable than the starting adduct complex. This conforms with the finding of Latimer et al.[79] for $[Cu_2O]^{2+}$. It gradually becomes less stable as we proceed from Cu (endothermic by +13.6 kcal/mol) to Ti (endothermic by +65.9 kcal/mol). The separated-methyl intermediates of $[Cu-O-Cr]^{2+}$, $[Cu-O-V]^{2+}$ and $[Cu-O-Ti]^{2+}$ are so unstable that there is really no point considering the associated transition states. Indeed, for these species, we

Table 4: Relative energies (kcal/mol) of the intermediates formed after methane C-H activation by various [Cu-O-M]$^{2+}$ active sites. The associated transition state barriers are given in parenthesis.

	Separated CH$_3$	Surface-stabilized CH$_3$		Separated CH$_3$	Surface-stabilized CH$_3$
Cu	+13.6 (19.9)	-10.4 (15.6)	Ag	+4.5 (5.0)	-15.1 (5.1)
Ni	+21.6 (23.5)	-13.4 (24.0)	Pd	+19.2 (20.0)	-24.6 (20.1)
Co	+24.2 (25.5)	-9.7 (28.1)	Rh		-12.5 (9.1)
Fe	+28.3 (28.7)	-2.7 (30.3)	Ru		-5.1 (24.7)
Mn	+29.1 (29.9)	-4.8 (30.9)			
Cr	+43.4	+1.5 (42.7)	Mo		+7.9
V	+53.0	+4.0	Nb		+13.8
Ti	+65.9	+7.9	Zr		+7.6

were not able to obtain the transition states for the surface-stabilized and separated-methyl mechanisms. The resulting barriers are sure to be high enough to prohibit methane activation at 200 °C. This is the case regardless of which spin state we considered. For these species, the barriers preclude methane activation at 200 °C, Table 4. Thus, while [Cu-O-Cr]$^{2+}$, [Cu-O-V]$^{2+}$ and [Cu-O-Ti]$^{2+}$ are interesting from a stability perspective (activation temperatures), they are nonetheless not useful as they are unreactive at the moderate temperatures that favor methanol selectivity.

For [Cu$_2$O]$^{2+}$, the barriers for the radical-like and surface-stabilized mechanisms are 19.9 and 15.6 kcal/mol, respectively, Table 4. These barriers indicate that [Cu$_2$O]$^{2+}$ can activate methane at 200 °C. For the heterometallic Ni, Co, Fe and Mn species, the magnitudes of the barriers for both mechanisms also indicate the ability to activate methane at 200 °C. The barriers follow the trend Cu < Ni < Co < Fe ~ Mn, Table 4.
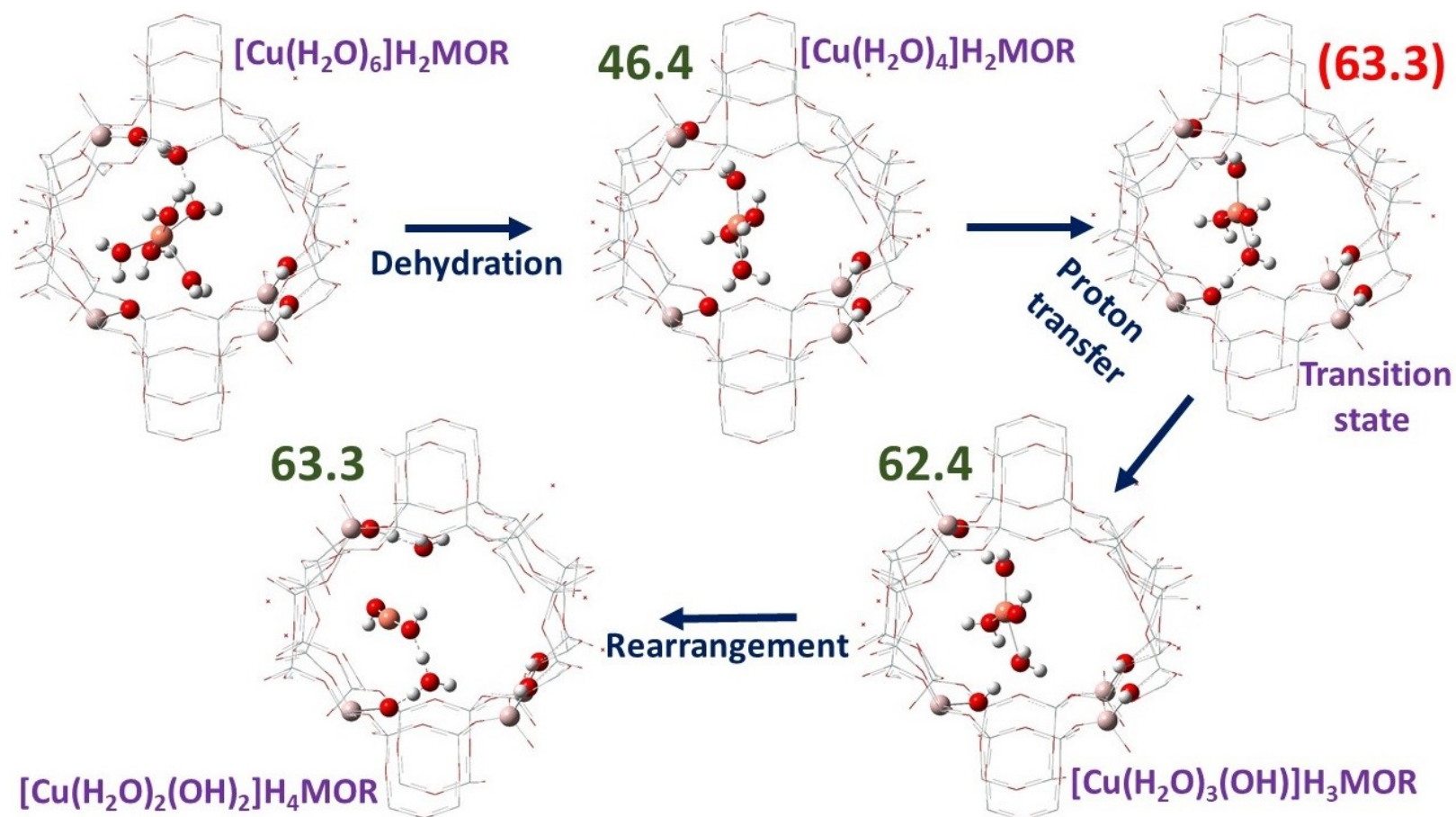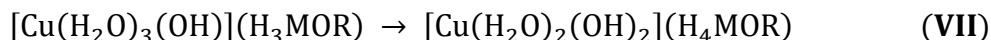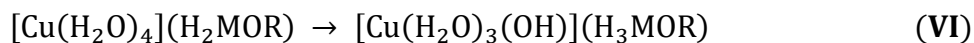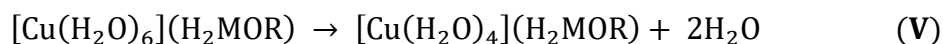
For 4d transition metals, the energies of the surface-stabilized intermediates for [Cu-O-Mo]$^{2+}$, [Cu-O-Nb]$^{2+}$ and [Cu-O-Zr]$^{2+}$ are either similar or more positive than those of their 3d analogues. Thus, these species are also likely unreactive. For these species, we were not able to obtain the separated-methyl intermediates as well as the transition states involved in the surface-stabilized mechanism. Overall, the calculated barriers indicate that only [Cu$_2$O]$^{2+}$, [Cu-O-Ni]$^{2+}$, [Cu-O-Co]$^{2+}$, [Cu-O-Fe]$^{2+}$, [Cu-O-Mn]$^{2+}$ [Cu-O-Ag]$^{2+}$, [Cu-O-Pd]$^{2+}$, [Cu-O-Rh]$^{2+}$ and [Cu-O-Ru]$^{2+}$ can activate methane at 200 °C. Of these, only [Cu-O-Rh]$^{2+}$ and [Cu-O-Ru]$^{2+}$ have formation energies that are lower than for [Cu$_2$O]$^{2+}$, respectively 10.6 and 6.2 kcal/mol in Figure 4. With a likely error bar of ±15 kcal/mol in the formation energies, it is unlikely that [Cu-O-Rh]$^{2+}$ and [Cu-O-Ru]$^{2+}$ can be formed at substantially lower temperatures than [Cu$_2$O]$^{2+}$. Their methane C-H activation barriers are also somewhat higher than that of [Cu$_2$O]$^{2+}$, suggesting lower methane conversions at 200 °C,

Table 4. The only great advantage that $[Cu-O-Rh]^{2+}$ and $[Cu-O-Ru]^{2+}$ have over $[Cu_2O]^{2+}$ lies in their greater resistance to autoreduction via O_2 elimination, Table 3. On the other hand, $[Cu-O-Ag]^{2+}$ provides significantly lower C-H activation barriers than $[Cu_2O]^{2+}$. However, it will be formed at nearly the same temperature as $[Cu_2O]^{2+}$, due to similar formation energies, Figure 4. It would also be more susceptible to autoreduction via O_2 elimination, Table 3. Lastly, considering the difficulties associated with potential synthesis routes for $[Cu-O-Rh]^{2+}$, $[Cu-O-Ru]^{2+}$ and $[Cu-O-Ru]^{2+}$ as well as the costs of Rh, Ru and Ag, one can only conclude that $[Cu_2O]^{2+}$ is the best suited bis(μ-oxo) dinuclear active site for methane activation under moderate reaction conditions.

3.5. Formation Mechanism of $[Cu_2O]^{2+}$ Sites: Having shown that $[Cu_2O]^{2+}$ is the optimal balance between formation energies, methane C-H reactivity, autoreduction and cost, we now turn to the mechanism by which this species is formed from hexaaquo Cu^{2+} species. Interestingly, the mechanism for formation of copper active sites has been experimentally investigated. [36, 60, 61, 63, 72, 80-83] It is understood that dissociation of water molecules transforms the $[Cu(H_2O)_6]^{2+}$ complex to hydroxylated $[Cu(H_2O)_x(OH)]^+$ species. These findings will guide our description of a plausible mechanism for forming the $[Cu_2O]^{2+}$ active site, in the absence of O_2 or other oxidants. As written in **I**, the Cu^{2+} sites of two $[Cu(H_2O)_6](H_2MOR)$ unit cells need to be dehydrated prior to formation of $[Cu_2O]^{2+}$. We repeat again that **I** is the overall formation reaction. Additionally, we will carry out dissociation of water in one unit cell while the other cell remains unchanged. The hydroxylated Cu species from water dissociation then migrates to condensate with the unchanged Cu center. By doing this, we are implying that migration of Cu ions within the zeolitic framework is crucial to formation of the active sites. We are also implying that reduction of some of the Cu centers (via water dissociation and formation of hydroxyl ligands) is essential for migration. These resonate *clearly* with previous experimental reports.[62]

For $[Cu(H_2O)_6](H_2MOR)$, initial loss of two aquo ligands leads to $[Cu(H_2O)_4](H_2MOR)$, **V**. This is an endothermic process, 46.4 kcal/mol. Subsequently, transfer of a proton from an aquo ligand to a framework aluminate leads to formation of $[Cu(H_2O)_3(OH)](H_3MOR)$, **VI**. This step is also endothermic, by 16.0 kcal/mol and has a reaction barrier of 16.9 kcal/mol. The low reaction barrier is due to a network-like stabilization of the aquo protons, Figure 5. The central copper complex of $[Cu(H_2O)_3(OH)](H_3MOR)$ then rearranges to form a species reminiscent of $[Cu(H_2O)_2(OH)_2]$, **VII**. This step costs only 0.6 kcal/mol. In $[Cu(H_2O)_2(OH)_2](H_4MOR)$, both water molecules stabilize the two protons transferred to the framework, Figure 5. By transferring both protons, the

framework is converted from H₂MOR to H₄MOR. In other words, the charges of all four aluminates in the unit cell are now balanced with protons, Figure 5. H₄MOR is one of the final products of reaction **I**.
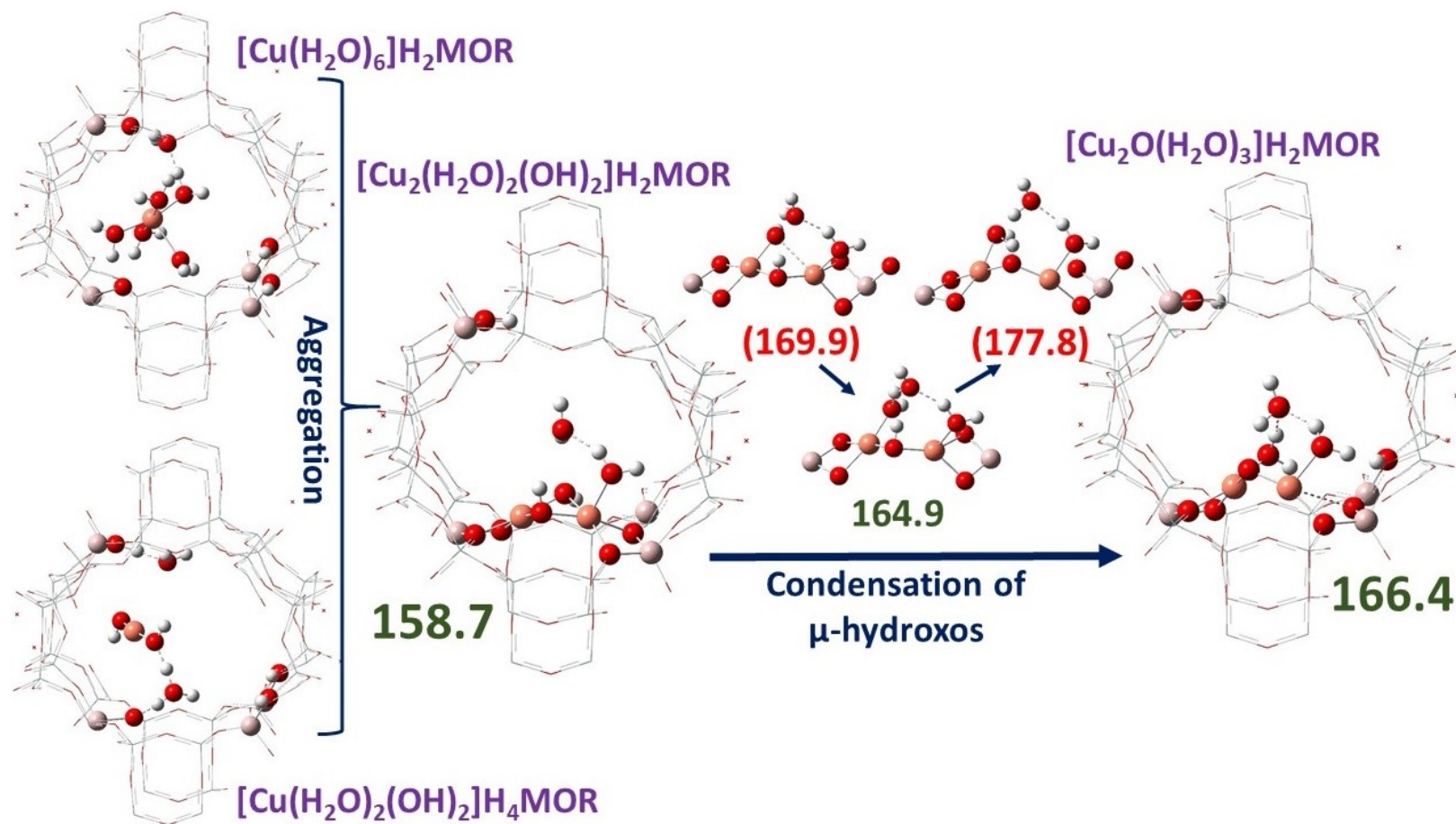
$$[Cu(H_2O)_6](H_2MOR) \rightarrow [Cu(H_2O)_4](H_2MOR) + 2H_2O \qquad \textbf{(V)}$$

$$[Cu(H_2O)_4](H_2MOR) \rightarrow [Cu(H_2O)_3(OH)](H_3MOR) \qquad \textbf{(VI)}$$

$$[Cu(H_2O)_3(OH)](H_3MOR) \rightarrow [Cu(H_2O)_2(OH)_2](H_4MOR) \qquad \textbf{(VII)}$$

Figure 5: Pathway for hexaaquo core of $[Cu(H_2O)_6](H_2MOR)$ during formation of $[Cu_2O]^{2+}$ sites. Reaction energies are given in green and kcal/mol. Barriers are given in red and parenthesis. These are all relative to $[Cu(H_2O)_6](H_2MOR)$. The four aluminates of the unit cell are also shown.

Examination of the $[Cu(H_2O)_2(OH)_2]$ group in $[Cu(H_2O)_2(OH)_2](H_4MOR)$ shows that it can diffuse along the main channel to adjacent 8MRs. As the $[Cu(H_2O)_2(OH)_2]$ group migrates from its cell, it leaves behind H₄MOR. The migrating moiety can coalesce with the $[Cu(H_2O)_6]^{2+}$ core of a $[Cu(H_2O)_6](H_2MOR)$ unit cell. In this process, the six aquo ligands of the $[Cu(H_2O)_6]^{2+}$ core are eliminated, **VIII**. This combined aggregation and dehydration step brings the overall reaction energy to 158.7 kcal/mol and leads to $[Cu_2(H_2O)_2(OH)_2](H_2MOR)$, which possesses a dinuclear

core with two μ-hydroxo groups, Figure 6. In summary, reactions **V-VIII** are a series of water-dissociation steps to form Cu-hydroxyl species, migration of these Cu-hydroxyl centers and finally condensation of the Cu-hydroxyl species to framework aluminate tetrahedra.[62]

$$[Cu(H_2O)_2(OH)_2](H_4MOR) + [Cu(H_2O)_6](H_2MOR)$$

$$\rightarrow H_4MOR + [Cu_2(H_2O)_2(OH)_2](H_2MOR) + 6H_2O \qquad (\mathbf{VIII})$$

$$[Cu_2(H_2O)_2(OH)_2](H_2MOR) \rightarrow [Cu_2O(H_2O)_3](H_2MOR) \qquad (\mathbf{IX})$$
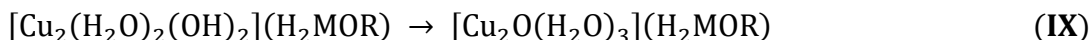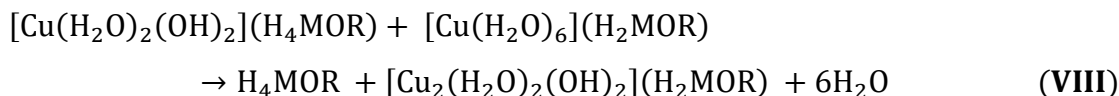
Figure 6: Aggregation and dehydration steps during formation of $[Cu_2O]^{2+}$. Reaction energies are given in green and kcal/mol. Barriers are given in red and parenthesis. These are all relative to two $[Cu(H_2O)_6](H_2MOR)$ reactants. Details of the condensation of μ-hydroxo groups are shown.

Condensation of the two hydroxo groups leads to a mono-(μ-oxo) bridge between the copper centers and an aquo group, **IX**. This condensation costs 7.5 kcal/mol and brings the total reaction energy to 166.4 kcal/mol. However, the condensation proceeds in two steps, first breaking of a μ(OH)-Cu bond to create a dangling hydroxo group and second, a proton transfer from the μ-hydroxo to the dangling hydroxo. The OH-Cu scission step costs 6.2 kcal/mol while the proton
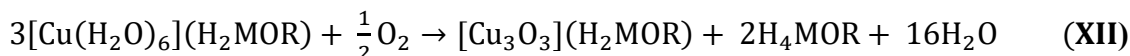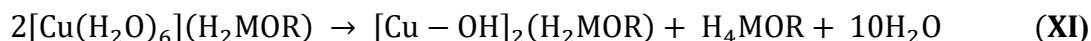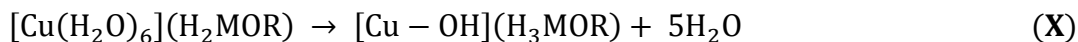
transfer step costs 1.3 kcal/mol. These OH-Cu scission and proton transfer steps have transition state barriers of 11.2 and 12.9 kcal/mol, respectively. Loss of three aquo ligands from $[Cu_2O(H_2O)_3](H_2MOR)$ leads to $[Cu_2O](H_2MOR)$, in which the charges of two aluminate groups are balanced by the $[Cu_2O]^{2+}$ site. This dehydration step brings the overall reaction energy to 222.5 kcal/mol, Table 2.

Our results, Figures 4 and 5, reveal that dehydration steps are the most energy-consuming portions of the formation pathway for $[Cu_2O]^{2+}$. Additionally, $[Cu_2O]^{2+}$ is formed via condensation of two hydroxo groups formed by proton transfer to framework aluminates. Thus, the μ-oxo atom of $[Cu_2O]^{2+}$ originates from water, rather than oxidants like O_2 or N_2O.[63, 72] Lastly, transition states for the proton transfer and hydroxo condensation steps are stabilized greatly by hydrogen interactions with nearby water molecules. This further supports the crucial role of water during formation of the copper-oxo site. Overall, the calculated mechanism conforms to the experimental observations of Lamberti et al.[63]

3.6. Free-energy corrections and comparison to other copper-oxo sites: The calculated electronic formation energy for $[Cu_2O]^{2+}$ via **I** is 222.5 kcal/mol at the periodic PBE-D3 level, Table 2. Also, although all transition states are only 11.3-16.9 kcal/mol above their intermediates, it is crucial to note that the highest-energy transition state in the mechanism for $[Cu_2O]^{2+}$ formation is 177.8 kcal/mol above the initial $[Cu(H_2O)_6](H_2MOR)$ reactants, Figures 4 and 5. It becomes important that we consider Gibbs free-energy corrections, at least to the overall reaction energies. Additionally, comparing the formation free-energy of $[Cu_2O]^{2+}$ to those of $[Cu_3O_3]^{2+}$, isolated [Cu-OH]$^+$ and paired or dinuclear [Cu-OH]$^+$ will provide insights into its relationships with other highly active copper-oxo species.

In our previous work, we showed that we could obtain reasonable estimates of the reaction free-energies.[24] We did this by considering only free-energy corrections for the central $[Cu(H_2O)_6]^{2+}$ core of $[Cu(H_2O)_6](H_2MOR)$ and the eliminated water molecules. To further refine our approach, we here obtain the free-energy corrections using cluster-models that are representative of the MOR unit cell, see Supporting Information. The formation energies of, isolated [Cu-OH]$^+$, paired [Cu-OH]$^+$ and $[Cu_3O_3]^{2+}$ are calculated according to **X-XII**.

$$[Cu(H_2O)_6](H_2MOR) \rightarrow [Cu-OH](H_3MOR) + 5H_2O \qquad \textbf{(X)}$$

$$2[Cu(H_2O)_6](H_2MOR) \rightarrow [Cu-OH]_2(H_2MOR) + H_4MOR + 10H_2O \qquad \textbf{(XI)}$$

$$3[Cu(H_2O)_6](H_2MOR) + \tfrac{1}{2}O_2 \rightarrow [Cu_3O_3](H_2MOR) + 2H_4MOR + 16H_2O \qquad \textbf{(XII)}$$

17

In Table 5, we present the formation energies of $[Cu_2O]^{2+}$, $[Cu_3O_3]^{2+}$, isolated $[Cu\text{-}OH]^+$ and paired $[Cu\text{-}OH]^+$ obtained with periodic DFT and cluster-model calculations. The formation energies follow the trend: isolated $[Cu\text{-}OH]^+ <$ paired $[Cu\text{-}OH]^+ < [Cu_2O]^{2+} < [Cu_3O_3]^{2+}$. This matches well with the fact that 5, 10, 11 and 16 water molecules are released during the formation of isolated $[Cu\text{-}OH]^+$, paired $[Cu\text{-}OH]^+$, $[Cu_2O]^{2+}$ and $[Cu_3O_3]^{2+}$ respectively. Also, the formation energies obtained from the cluster models are higher than those from periodic DFT, Table 5. This is likely because the cluster models are not able to capture long-range relaxation effects that occur in the crystal lattice after introduction of the copper active sites. However, the terminating protons of all model species in **I** and **X-XII** are fixed at exactly the same positions. As such, we expect the Gibbs free-energy corrections for these reactions to be quite useful, Figure 7.

Table 5: Energies, kcal/mol, for formation of $[Cu_2O]^{2+}$, $[Cu_3O_3]^{2+}$, isolated $[Cu\text{-}OH]^+$ and paired $[Cu\text{-}OH]^+$ active sites. The temperatures at which ΔG becomes 0.0 kcal/mol are given in °C.

		$[Cu_2O]^{2+}$	$[Cu_3O_3]^{2+}$	$[Cu\text{-}OH]^+$	
				Isolated	Dinuclear/paired
Periodic structure: PBE-D3	ΔE	222.5	348.1	106.7	190.2
Cluster-model: PBE	ΔE	264.1	361.0	110.2	232.2
	ΔG at 25 °C	123.1	170.0	43.9	103.5
	Temp. for ΔG=0	327	331	257	297

There are several important things to note regarding results in Table 5 and Figure 7. First, paired $[Cu\text{-}OH]^+$, $[Cu_2O]^{2+}$ and $[Cu_3O_3]^{2+}$ have formation energies of 232.2, 264.1 and 361.0 kcal/mol, respectively, from cluster-model DFT. By considering the free-energy corrections, these species are expected to be formed at 297, 327 and 331 °C, respectively. However, there is likely an error bar of ±15 kcal/mol in the calculated formation energies, as discussed earlier. Thus, paired $[Cu\text{-}OH]^+$, $[Cu_2O]^{2+}$ and $[Cu_3O_3]^{2+}$ can be formed at 267-347, 285-357 and 300-354 °C, respectively, Figure 7. These ranges are compatible with typical experimental protocols. Additionally, these temperature ranges suggest that paired $[Cu\text{-}OH]^+$, $[Cu_2O]^{2+}$ and $[Cu_3O_3]^{2+}$ can co-exist or compete under certain conditions. We note that a recent report by Knorpp et al. identified paired $[Cu\text{-}OH]^+$ as the active site species in zeolite omega.[84]

Second, for isolated $[Cu\text{-}OH]^+$ species, the formation energy is 110.2 kcal/mol from the cluster-model calculations. Free-energy corrections indicate that this species will be formed at 257 °C. This is quite low. Such a low activation temperature implicates isolated $[Cu\text{-}OH]^+$ as a precursor for other copper active sites. This is consistent with the mechanism presented in Figure 6, where

$[Cu_2O]^{2+}$ is formed from ion pairs of $[Cu-OH]^+$ as $[Cu_2(H_2O)_2(OH)_2](H_2MOR)$ species. The low activation temperature also implicate $[Cu-OH]^+$ in previous isothermal MMC experiments near 200 °C.[85-87] This is particularly interesting given Kulkarni et al.'s report that $[Cu-OH]^+$ activates the methane C-H bond with a barrier of 26.3 kcal/mol.[88] However, we emphasize that our calculations are relatively simple models of rather complex zeolite synthesis systems. We are also using the reaction thermodynamics to obtain insights into the activation temperatures. An error bar of ±15 kcal/mol in the formation energies implies that isolated $[Cu-OH]^+$ species will definitely be formed between 177 and 337 °C, Figure 7. It is thus quite likely that the active sites responsible for MMC in the isothermal MMC experiments are hydrated $[Cu-OH]^+$ species.
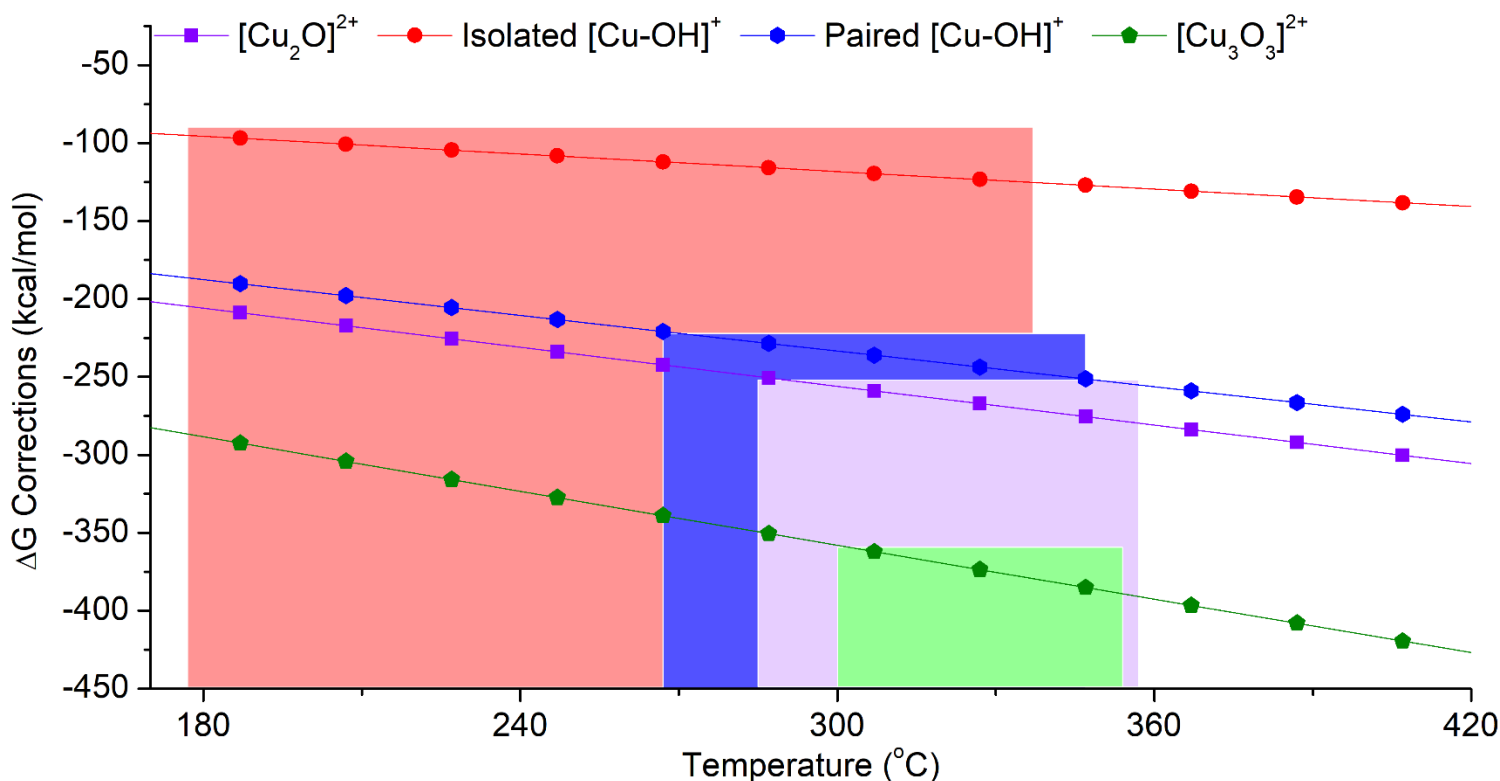
Figure 7: Temperature-dependent free-energy corrections for formation of copper active sites in zeolite MOR. The shaded regions represent ±15 kcal/mol around the electronic formation energies.

4. CONCLUSIONS

Using scalar-relativistic periodic DFT, nudged elastic band and representative cluster-model calculations, we have investigated the formation energies of $[Cu_2O]^{2+}$ and its heterometallic [Cu-O-M]$^{2+}$ analogues (where (M = Ti-Cu, Zr-Mo and Ru-Ag) in the eight-membered ring of zeolite mordenite, MOR. The heterometallic active site motifs are interesting from the perspective of mimicking the multi-metal centers of some metalloenzymes. We here use DFT calculations to

examine their properties, prior to future experimental preparations and characterizations which might prove tedious and expensive. Particularly, the susceptibilities of these active site motifs to autoreduction by O_2 elimination as well as their reactivities with the methane C-H bond were also investigated. A mechanism for the formation of $[Cu_2O]^{2+}$ from copper-aquo species was provided. Lastly, to refine the absolute electronic energies obtained in this work, we calculated temperature-dependent Gibbs free-energy corrections. These are useful for estimating the activation temperatures of copper active sites and provide us a framework for comparing $[Cu_2O]^{2+}$ to isolated $[Cu\text{-}OH]^+$, paired $[Cu\text{-}OH]^+$ and $[Cu_3O_3]^{2+}$.

Our findings can be summarized thus:

1) The calculated formation energies divide the dinuclear active sites into two classes. On the one hand are $[Cu\text{-}O\text{-}Cr]^{2+}$, $[Cu\text{-}O\text{-}V]^{2+}$, $[Cu\text{-}O\text{-}Ti]^{2+}$, $[Cu\text{-}O\text{-}Mo]^{2+}$, $[Cu\text{-}O\text{-}Nb]^{2+}$, $[Cu\text{-}O\text{-}Zr]^{2+}$, which are substantially more stable than $[Cu_2O]^{2+}$. These species will be expected to form at much lower temperatures than $[Cu_2O]^{2+}$. On the other hand are $[Cu\text{-}O\text{-}Mn]^{2+}$, $[Cu\text{-}O\text{-}Fe]^{2+}$, $[Cu\text{-}O\text{-}Co]^{2+}$, $[Cu\text{-}O\text{-}Ni]^{2+}$, $[Cu\text{-}O\text{-}Ru]^{2+}$, $[Cu\text{-}O\text{-}Rh]^{2+}$, $[Cu\text{-}O\text{-}Pd]^{2+}$ and $[Cu\text{-}O\text{-}Ag]^{2+}$ which have similar formation energies as $[Cu_2O]^{2+}$, to within 10 kcal/mol.

2) The autoreduction energies via O_2 elimination indicate that only $[Cu\text{-}O\text{-}Pd]^{2+}$ and $[Cu\text{-}O\text{-}Ag]^{2+}$ are more susceptible towards autoreduction than $[Cu_2O]^{2+}$.

3) The C-H activation barrier was used to characterize the reactivities of the dinuclear active sites towards methane. Based on the calculated barriers, only $[Cu_2O]^{2+}$, $[Cu\text{-}O\text{-}Mn]^{2+}$, $[Cu\text{-}O\text{-}Fe]^{2+}$, $[Cu\text{-}O\text{-}Co]^{2+}$, $[Cu\text{-}O\text{-}Ni]^{2+}$, $[Cu\text{-}O\text{-}Ru]^{2+}$, $[Cu\text{-}O\text{-}Rh]^{2+}$, $[Cu\text{-}O\text{-}Pd]^{2+}$ and $[Cu\text{-}O\text{-}Ag]^{2+}$ are useful for methane C-H activation at 200 °C. Only $[Cu\text{-}O\text{-}Ag]^{2+}$ provides barriers lower than that of $[Cu_2O]^{2+}$. All other species (Ti-Cr and Zr-Mo) provide prohibitively high reaction barriers for methane activation at this temperature.

4) Based on the formation energies, autoreduction energies, cost and methane C-H bond reactivities, we can only conclude that $[Cu_2O]^{2+}$ is best suited for methane-to-methanol conversion (MMC).

5) The mechanism for forming $[Cu_2O]^{2+}$ from copper hexaaquo species was described. The reaction proceeds via proton transfer from the aquo ligands to aluminates. This is followed by migration of a $Cu(OH)_2$-type moiety to another unit cell where it aggregates with Cu^{2+} to form a dinuclear bis(μ-hydroxo) species. Condensation of the hydroxo linkers is assisted by the proton-network of neighboring water molecules.

6) Gibbs free-energy corrections to the calculated formation energies of isolated $[Cu\text{-}OH]^+$, paired $[Cu\text{-}OH]^{2+}$, $[Cu_2O]^{2+}$ and $[Cu_3O_3]^{2+}$ reveal that these species will be formed around 257, 297, 327 and 331 °C, respectively. Thus, these dicopper and tricopper species can co-exist and compete under certain conditions. The estimated activation temperature for isolated $[Cu\text{-}OH]^+$ is very low. This indicates that $[Cu\text{-}OH]^+$ is a precursor for other copper active sites. The low activation temperature also suggests that $[Cu\text{-}OH]^+$ is likely involved in isothermal MMC experiments. By examining the limitations of our calculations, we conclude that isolated $[Cu\text{-}OH]^+$ sites would definitely be formed between 170 and 340 °C and that the species involved in isothermal MMC experiments are most likely hydrated forms of isolated or paired $[Cu\text{-}OH]^+$.

Conflicts of interest

The authors declare no conflict of interest.

Acknowledgements

References

1. G. A. Olah, *Angewandte Chemie International Edition*, 2005, **44**, 2636-2639.
2. J. H. Lunsford, *Catalysis Today*, 2000, **63**, 165-174.
3. J. Rostrup-Nielsen, France, 2004.
4. A. Holmen, *Catalysis Today*, 2009, **142**, 2-8.
5. P. Tang, Q. Zhu, Z. Wu and D. Ma, *Energy & Environmental Science*, 2014, **7**, 2580-2591.
6. K. Li, H. Wang and Y. Wei, *Journal of Chemistry*, 2013, **2013**, 294817.
7. M. Álvarez, P. Marín and S. Ordóñez, *Molecular Catalysis*, 2020, **487**, 110886.
8. N. V. Beznis, B. M. Weckhuysen and J. H. Bitter, *Catalysis Letters*, 2010, **138**, 14-22.
9. S. E. Bozbag, P. Sot, M. Nachtegaal, M. Ranocchiari, J. A. van Bokhoven and C. Mesters, *ACS Catalysis*, 2018, **8**, 5721-5731.
10. C. Hammond, M. M. Forde, M. H. Ab Rahim, A. Thetford, Q. He, R. L. Jenkins, N. Dimitratos, J. A. Lopez-Sanchez, N. F. Dummer, D. M. Murphy, A. F. Carley, S. H. Taylor, D. J. Willock, E. E. Stangland, J. Kang, H. Hagen, C. J. Kiely and G. J. Hutchings, *Angewandte Chemie-International Edition*, 2012, **51**, 5129-5133.
11. C. Hammond, R. L. Jenkins, N. Dimitratos, J. A. Lopez-Sanchez, M. H. ab Rahim, M. M. Forde, A. Thetford, D. M. Murphy, H. Hagen, E. E. Stangland, J. M. Moulijn, S. H. Taylor, D. J. Willock and G. J. Hutchings, *Chemistry-a European Journal*, 2012, **18**, 15735-15745.
12. M. O. Ross, F. MacMillan, J. Wang, A. Nisthal, T. J. Lawton, B. D. Olafson, S. L. Mayo, A. C. Rosenzweig and B. M. Hoffman, *Science*, 2019, **364**, 566.
13. B. E. R. Snyder, M. L. Bols, R. A. Schoonheydt, B. F. Sels and E. I. Solomon, *Chemical Reviews*, 2018, **118**, 2718-2768.

14. R. Balasubramanian, S. M. Smith, S. Rawat, L. A. Yatsunyk, T. L. Stemmler and A. C. Rosenzweig, *Nature*, 2010, **465**, 115-119.
15. L. Frunz, R. Prins and G. D. Pirngruber, *Chemistry of Materials*, 2007, **19**, 4357-4366.
16. A. W. Petrov, D. Ferri, O. Krocher and J. A. van Bokhoven, *Acs Catalysis*, 2019, **9**, 2303-2312.
17. M. B. Park, S. H. Ahn, A. Mansouri, M. Ranocchiari and J. A. van Bokhoven, *ChemCatChem*, 2017, **9**, 3705-3713.
18. M. H. Mahyuddin, Y. Shiota and K. Yoshizawa, *Catalysis Science & Technology*, 2019, **9**, 1744-1768.
19. Z.-J. Zhao, A. Kulkarni, L. Vilella, J. K. Nørskov and F. Studt, *ACS Catalysis*, 2016, **6**, 3760-3766.
20. E. M. Alayon, M. Nachtegaal, M. Ranocchiari and J. A. van Bokhoven, *Chemical Communications*, 2012, **48**, 404-406.
21. J. Zheng, I. Lee, E. Khramenkova, M. Wang, B. Peng, O. Y. Gutiérrez, J. L. Fulton, D. M. Camaioni, R. Khare, A. Jentys, G. L. Haller, E. A. Pidko, M. Sanchez-Sanchez and J. A. Lercher, *Chemistry – A European Journal*, 2020, **26**, 7563-7567.
22. M. Dyballa, K. Thorshaug, D. K. Pappas, E. Borfecchia, K. Kvande, S. Bordiga, G. Berlier, A. Lazzarini, U. Olsbye, P. Beato, S. Svelle and B. Arstad, *ChemCatChem*, 2019, **11**, 5022-5026.
23. V. L. Sushkevich and J. A. van Bokhoven, *Catalysis Science & Technology*, 2018, **8**, 4141-4150.
24. O. Suleiman, O. Adeyiga, D. Panthi and S. O. Odoh, *The Journal of Physical Chemistry C*, 2021, **125**, 6684-6693.
25. O. Adeyiga and S. O. Odoh, *Chemphyschem*, 2021, **22**, 1101-1109.
26. M. A. Newton, A. J. Knorpp, V. L. Sushkevich, D. Palagin and J. A. van Bokhoven, *Chemical Society Reviews*, 2020, **49**, 1449-1486.
27. M. H. Groothaert, P. J. Smeets, B. F. Sels, P. A. Jacobs and R. A. Schoonheydt, *Journal of the American Chemical Society*, 2005, **127**, 1394-1395.
28. Z. Liu, E. Huang, I. Orozco, W. Liao, R. M. Palomino, N. Rui, T. Duchoň, S. Nemšák, D. C. Grinter, M. Mahapatra, P. Liu, J. A. Rodriguez and S. D. Senanayake, *Science*, 2020, **368**, 513.
29. K. Curtis, D. Panthi and S. O. Odoh, *Inorganic Chemistry*, 2021, **60**, 1149-1159.
30. A. Martini, M. Signorile, C. Negri, K. Kvande, K. A. Lomachenko, S. Svelle, P. Beato, G. Berlier, E. Borfecchia and S. Bordiga, *Physical Chemistry Chemical Physics*, 2020, **22**, 18950-18963.
31. E. Borfecchia, D. K. Pappas, M. Dyballa, K. A. Lomachenko, C. Negri, M. Signorile and G. Berlier, *Catalysis Today*, 2019, **333**, 17-27.
32. E. Borfecchia, P. Beato, S. Svelle, U. Olsbye, C. Lamberti and S. Bordiga, *Chemical Society Reviews*, 2018, **47**, 8097-8133.
33. M. A. Newton, A. J. Knorpp, A. B. Pinar, V. L. Sushkevich, D. Palagin and J. A. van Bokhoven, *Journal of the American Chemical Society*, 2018, **140**, 10090-10093.
34. O. Suleiman, D. Panthi, O. Adeyiga and S. O. Odoh, *Inorganic Chemistry*, 2021, DOI: 10.1021/acs.inorgchem.0c03279, accepted.
35. A. A. Kolganov, A. A. Gabrienko, S. A. Yashnik, E. A. Pidko and A. G. Stepanov, *The Journal of Physical Chemistry C*, 2020, **124**, 6242-6252.
36. S. Grundner, M. A. C. Markovits, G. Li, M. Tromp, E. A. Pidko, E. J. M. Hensen, A. Jentys, M. Sanchez-Sanchez and J. A. Lercher, *Nature Communications*, 2015, **6**, 7546.
37. M. H. Mahyuddin, T. Tanaka, A. Staykov, Y. Shiota and K. Yoshizawa, *Inorganic Chemistry*, 2018, **57**, 10146-10152.
38. B. E. R. Snyder, M. L. Bols, R. A. Schoonheydt, B. F. Sels and E. I. Solomon, *Chem Rev*, 2018, **118**, 2718-2768.
39. P. Hohenberg and W. Kohn, *Physical Review*, 1964, **136**, B864-B871.
40. W. Kohn and L. J. Sham, *Phys. Rev.*, 1965, **140**, A1133-A1138.
41. G. Wang, L. Huang, W. Chen, J. Zhou and A. Zheng, *Physical Chemistry Chemical Physics*, 2018, **20**, 26522-26531.

42.   L. Wang, Z. Li, Z. Wang, X. Chen, W. Song, Z. Zhao, Y. Wei and X. Zhang, *Industrial & Engineering Chemistry Research*, 2021, **60**, 2400-2409.

43.   A. R. Kulkarni, Z.-J. Zhao, S. Siahrostami, J. K. Nørskov and F. Studt, *Catalysis Science & Technology*, 2018, **8**, 114-123.

44.   P. Tomkins, A. Mansouri, S. E. Bozbag, F. Krumeich, M. B. Park, E. M. C. Alayon, M. Ranocchiari and J. A. van Bokhoven, *Angewandte Chemie International Edition*, 2016, **55**, 5467-5471.

45.   P. Buchwalter, J. Rose and P. Braunstein, *Chemical Reviews*, 2015, **115**, 28-126.

46.   M. Can, F. A. Armstrong and S. W. Ragsdale, *Chemical Reviews*, 2014, **114**, 4149-4174.

47.   S. A. Cook, E. A. Hill and A. S. Borovik, *Biochemistry*, 2015, **54**, 4167-4180.

48.   I. Garcia-Bosch, X. Ribas and M. Costas, *European Journal of Inorganic Chemistry*, 2012, DOI: 10.1002/ejic.201100957, 179-187.

49.   Y. Lyu, J. N. Jocz, R. Xu, O. C. Williams and C. Sievers, *Chemcatchem*, DOI: 10.1002/cctc.202100268.

50.   S. Van de Vyver and Y. Roman-Leshkov, *Angewandte Chemie-International Edition*, 2015, **54**, 12554-12561.

51.   P. Giannozzi, S. Baroni, N. Bonini, M. Calandra, R. Car, C. Cavazzoni, D. Ceresoli, G. L. Chiarotti, M. Cococcioni, I. Dabo, A. Dal Corso, S. de Gironcoli, S. Fabris, G. Fratesi, R. Gebauer, U. Gerstmann, C. Gougoussis, A. Kokalj, M. Lazzeri, L. Martin-Samos, N. Marzari, F. Mauri, R. Mazzarello, S. Paolini, A. Pasquarello, L. Paulatto, C. Sbraccia, S. Scandolo, G. Sclauzero, A. P. Seitsonen, A. Smogunov, P. Umari and R. M. Wentzcovitch, *Journal of Physics: Condensed Matter*, 2009, **21**, 395502.

52.   P. Giannozzi, O. Andreussi, T. Brumme, O. Bunau, M. Buongiorno Nardelli, M. Calandra, R. Car, C. Cavazzoni, D. Ceresoli, M. Cococcioni, N. Colonna, I. Carnimeo, A. Dal Corso, S. de Gironcoli, P. Delugas, R. A. DiStasio, A. Ferretti, A. Floris, G. Fratesi, G. Fugallo, R. Gebauer, U. Gerstmann, F. Giustino, T. Gorni, J. Jia, M. Kawamura, H. Y. Ko, A. Kokalj, E. Küçükbenli, M. Lazzeri, M. Marsili, N. Marzari, F. Mauri, N. L. Nguyen, H. V. Nguyen, A. Otero-de-la-Roza, L. Paulatto, S. Poncé, D. Rocca, R. Sabatini, B. Santra, M. Schlipf, A. P. Seitsonen, A. Smogunov, I. Timrov, T. Thonhauser, P. Umari, N. Vast, X. Wu and S. Baroni, *Journal of Physics: Condensed Matter*, 2017, **29**, 465901.

53.   K. D. Vogiatzis, G. Li, E. J. M. Hensen, L. Gagliardi and E. A. Pidko, *The Journal of Physical Chemistry C*, 2017, **121**, 22295-22302.

54.   P. E. Blöchl, *Physical Review B*, 1994, **50**, 17953-17979.

55.   G. Kresse and D. Joubert, *Physical Review B*, 1999, **59**, 1758-1775.

56.   J. P. Perdew, K. Burke and M. Ernzerhof, *Phys. Rev. Lett.*, 1996, **77**, 3865-3868.

57.   S. Grimme, J. Antony, S. Ehrlich and H. Krieg, *The Journal of Chemical Physics*, 2010, **132**, 154104.

58.   S. Grimme, S. Ehrlich and L. Goerigk, *Journal of Computational Chemistry*, 2011, **32**, 1456-1465.

59.   G. Henkelman, B. P. Uberuaga and H. Jónsson, *The Journal of Chemical Physics*, 2000, **113**, 9901-9904.

60.   E. M. C. Alayon, M. Nachtegaal, M. Ranocchiari and J. A. van Bokhoven, *Chimia*, 2012, **66**, 668-674.

61.   T. Ikuno, S. Grundner, A. Jentys, G. Li, E. Pidko, J. Fulton, M. Sanchez-Sanchez and J. A. Lercher, *The Journal of Physical Chemistry C*, 2019, **123**, 8759-8769.

62.   L. Tao, I. Lee and M. Sanchez-Sanchez, *Catalysis Science & Technology*, 2020, **10**, 7124-7141.

63.   F. X. Llabrés i Xamena, P. Fisicaro, G. Berlier, A. Zecchina, G. T. Palomino, C. Prestipino, S. Bordiga, E. Giamello and C. Lamberti, *The Journal of Physical Chemistry B*, 2003, **107**, 7036-7044.

64.   R. Sabatini, T. Gorni and S. de Gironcoli, *Physical Review B*, 2013, **87**, 041108.

65.   O. A. Vydrov and T. V. Voorhis, *The Journal of Chemical Physics*, 2010, **133**, 244103.

66.   I. Hamada, *Physical Review B*, 2014, **89**, 121103.

67.   D. N. Laikov, *Chemical Physics Letters*, 2005, **416**, 116-120.

68.   D. N. Laikov and Y. A. Ustynyuk, *Russian Chemical Bulletin*, 2005, **54**, 820-826.

69. D. N. Laikov, *Theoretical Chemistry Accounts*, 2019, **138**, 40.
70. D. N. Laikov, *The Journal of Chemical Physics*, 2020, **153**, 114121.
71. P. Vanelderen, B. E. R. Snyder, M.-L. Tsai, R. G. Hadt, J. Vancauwenbergh, O. Coussens, R. A. Schoonheydt, B. F. Sels and E. I. Solomon, *J. Am. Chem. Soc.*, 2015, **137**, 6383-6392.
72. B. Ipek, M. J. Wulfers, H. Kim, F. Göltl, I. Hermans, J. P. Smith, K. S. Booksh, C. M. Brown and R. F. Lobo, *ACS Catalysis*, 2017, **7**, 4291-4303.
73. G. Turnes Palomino, P. Fisicaro, S. Bordiga, A. Zecchina, E. Giamello and C. Lamberti, *The Journal of Physical Chemistry B*, 2000, **104**, 4064-4073.
74. O. Adeyiga, O. Suleiman and S. O. Odoh, *Inorganic Chemistry*, 2021, **60**, 8489-8499.
75. O. Suleiman, D. Panthi, O. Adeyiga and S. O. Odoh, *Inorganic Chemistry*, 2021, **60**, 6218-6227.
76. M. H. Mahyuddin, A. Staykov, Y. Shiota, M. Miyanishi and K. Yoshizawa, *ACS Catalysis*, 2017, **7**, 3741-3751.
77. A. A. Arvidsson, V. P. Zhdanov, P.-A. Carlsson, H. Grönbeck and A. Hellman, *Catalysis Science & Technology*, 2017, **7**, 1470-1477.
78. M. H. Mahyuddin, T. Tanaka, Y. Shiota, A. Staykov and K. Yoshizawa, *ACS Catalysis*, 2018, **8**, 1500-1509.
79. A. A. Latimer, A. R. Kulkarni, H. Aljama, J. H. Montoya, J. S. Yoo, C. Tsai, F. Abild-Pedersen, F. Studt and J. K. Nørskov, *Nature Materials*, 2017, **16**, 225-229.
80. C. W. Andersen, E. Borfecchia, M. Bremholm, M. R. V. Jørgensen, P. N. R. Vennestrøm, C. Lamberti, L. F. Lundegaard and B. B. Iversen, *Angewandte Chemie International Edition*, 2017, **56**, 10367-10372.
81. K. T. Dinh, M. M. Sullivan, K. Narsimhan, P. Serna, R. J. Meyer, M. Dincă and Y. Román-Leshkov, *Journal of the American Chemical Society*, 2019, **141**, 11641-11650.
82. S. Grundner, W. Luo, M. Sanchez-Sanchez and J. A. Lercher, *Chemical Communications*, 2016, **52**, 2553-2556.
83. Y. Kim, T. Y. Kim, H. Lee and J. Yi, *Chemical Communications*, 2017, **53**, 4116-4119.
84. A. J. Knorpp, A. B. Pinar, C. Baerlocher, L. B. McCusker, N. Casati, M. A. Newton, S. Checchia, J. Meyet, D. Palagin and J. A. van Bokhoven, *Angewandte Chemie International Edition*, 2021, **60**, 5854-5858.
85. J.-P. Lange, V. L. Sushkevich, A. J. Knorpp and J. A. van Bokhoven, *Industrial & Engineering Chemistry Research*, 2019, **58**, 8674-8680.
86. D. Palagin, V. L. Sushkevich and J. A. van Bokhoven, *ACS Catalysis*, 2019, **9**, 10365-10374.
87. V. L. Sushkevich, D. Palagin, M. Ranocchiari and J. A. van Bokhoven, *Science*, 2017, **356**, 523-527.
88. A. R. Kulkarni, Z.-J. Zhao, S. Siahrostami, J. K. Nørskov and F. Studt, *ACS Catalysis*, 2016, **6**, 6531-6536.

For Table of Contents Only
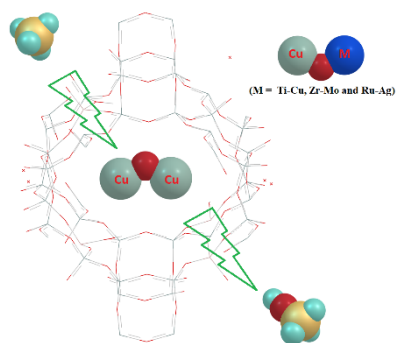
Synopsis: Formation energies and mechanisms, autoreduction and methane C-H reactivities were obtained for $[Cu-O-M]^{2+}$ species (M = Ti-Cu, Zr-Mo and Ru-Ag) in mordenite with DFT. These reveal that $[Cu_2O]^{2+}$ is best suited for MMC.